# Wavefield Modeling and Analysis of Lightning Quakes Measured by a Distributed Acoustic Sensing Array

Nolan Roth*[1], Tieyuan Zhu[1], Rafal Czarny[1], and Yongxin Gao[2]

## ABSTRACT

**Lightning-induced seismic waves, termed "lightning quakes," are frequent natural sources in many storm-prone regions. Lightning quakes have been clearly observed in numerous environments by both seismic and acoustic instruments, for example, by distributed acoustic sensing (DAS) array. Despite these numerous observations, the physical nature of lightning quake wavefields detected by ground-based arrays remains poorly understood. The possibility of electroseismic (ES) conversion due to lightning's powerful electromagnetic fields was, until now, unstudied. This investigation uses 3D numerical simulations of acoustic-to-seismic and ES wavefields alongside a novel data-driven azimuthal strain-rate variation analysis technique to robustly reveal the complex nature of lightning quakes. We show that lightning quakes begin as airborne acoustic waves before coupling with the solid earth as air-coupled Rayleigh waves and Love waves that are generated by local sources near the receiver, such as topography or urban infrastructure. These conclusions suggest thunder observations from a DAS array can be used to infer the structure of the near surface around the receiver, but care needs to be taken in understanding the role of local sources. An estimate of the Rayleigh- and Love-wave phase velocities is produced using a novel data analysis method unique to DAS. Furthermore, we demonstrate that electroseismic coupling does not play a significant role in the lightning quake wavefields. Although these simulations do not fully capture the realistic frequency of the electroseismic coupled wavefield, theory suggests that the wavefield is high frequency and thus quickly attenuated in the saturated near-surface soils. Electroseismic coupled wavefields from lightning may be detectable very close to the bolt.**

## KEY POINTS

- Electroseismic coupling of lightning is not observed by the Fiber Optic foR Environmental SEnsEing (FORESEE) distributed acoustic sensing (DAS) array.
- A novel analysis technique using DAS azimuthal sensitivity is demonstrated.
- Surface-wave phase velocity is inferred from azimuthal variations in DAS strain rates.

## INTRODUCTION

The seismic signals associated with lightning strikes, what we term "lightning quakes," have been studied for their applications in the characterization of the near-surface and the lightning itself. Lightning quakes have previously been recorded with surface seismometers (Kappus and Vernon, 1991; Lin and Langston, 2007, 2009a; Hinzen, 2012; Novoselov *et al.*, 2022), microphones (Lin and Langston, 2007, 2009a; Abegunawardana *et al.*, 2016; Lamb *et al.*, 2018), borehole seismometers (Kappus and Vernon, 1991; Lin and Langston, 2007, 2009a), and distributed acoustic sensing (DAS) arrays (Zhu and Stensrud, 2019; Hone and Zhu, 2021).

Complementary to seismic recordings of lightning quakes are the many measurements of the National Lightning Detection Network (NLDN) in the United States and the Austrian Lightning Detection and Information System in parts of central Europe (Novoselov *et al.*, 2022). The NLDN provides estimates of lightning strike time, peak current, polarity, cloud-to-ground classification, and location (Cummins *et al.*, 1998).

1. Department of Geosciences, Penn State University, State College, Pennsylvania, U.S.A., https://orcid.org/0000-0003-2587-2633 (NR); https://orcid.org/0000-0002-7463-3180 (RC); 2. Applied Institute of Mechanics, School of Civil Engineering, Hefei University of Technology, Hefei, China, https://orcid.org/0000-0002-7529-8329 (YG)

*Corresponding author: nolan.roth@psu.edu

**Cite this article as** Roth, N., T. Zhu, R. Czarny, and Y. Gao (2023). Wavefield Modeling and Analysis of Lightning Quakes Measured by a Distributed Acoustic Sensing Array, *Bull. Seismol. Soc. Am.* **XX**, 1–16, doi: 10.1785/0120230116

© Seismological Society of America



Downloaded from http://pubs.geoscienceworld.org/ssa/bssa/article-pdf/doi/10.1785/0120230116/5983977/bssa-2023116.1.pdf
by Pennsylvania State University user

Lightning strikes have been shown to create complex seismic responses with inconsistent frequency content depending on study methods and instrumentation (Novoselov *et al.*, 2022). Central frequencies range from 0.2 Hz (Dessler, 1973) to 200 Hz (Few, 1969) with many others reported in between (Few, 1969; Kitov *et al.*, 1997; Graneau, 1989; Lin and Langston, 2007, 2009a,b; Abegunawardana *et al.*, 2016; Zhu and Stensrud, 2019; Novoselov *et al.*, 2022).

Abegunawardana *et al.* (2016) showed that there may be multiple classifications of thunder, each with differing main frequency bands. Signals arriving directly from the thunder source are labeled as "peals" (~40–100 Hz) whereas "claps" (~40–160 Hz) and "rumbles" (~25–80 Hz) originate from peal reflections and distant lightning bolts, respectively. In any case, it can be agreed that lightning quakes are a very broadband phenomena.

Several key features of lightning are inherently tied to the observed complexity of lightning's seismic signature. First, it is extreme temperatures that cause the sudden expansion of the atmosphere around the channel, forming a shockwave that rapidly degenerates into an acoustic wave within several meters of the bolt (Graneau, 1989; Dwyer and Uman, 2014; Abegunawardana *et al.*, 2016; Beroual and Fofana, 2016; Blumenthal, 2016). The hottest section of the lightning bolt is typically at the altitude of its leader attachment point, often tens to hundreds of meters above the ground (Krider and Wetmore, 1987; Hill, 2012; Lu *et al.*, 2012; Dwyer and Uman, 2014; Tran *et al.*, 2014; Boggs *et al.*, 2021). Second, the geometry of the shockwave is not simple due to the dynamic nature of the lightning temperature and shape. The tortuosity of the bolt contorts the shockwave into semi-discrete spherical thunder sources in traditional "string-of-pearls" theory (Few, 1969). Third, the electrical power of lightning, measured as the peak current of the bolt, is directly correlated to the acoustic power of its thunder (Lin and Langston, 2007; Nieckarz *et al.*, 2011; Lu *et al.*, 2012; Dwyer and Uman, 2014; Beroual and Fofana, 2016; Zhu and Stensrud, 2019; Novoselov *et al.*, 2022). Typical peak currents are between five and several hundred kiloamps, with positively charged bolts generally being stronger.

The ground motions of lightning quakes show a similar complexity to their source function. The string-of-pearls thunder sources begin as shockwaves but degenerate into acoustic waves and couple with the ground through the mechanisms of acoustic-to-seismic ground coupling (Few, 1969; Novoselov *et al.*, 2020). Acoustic-to-seismic ground coupling is the focus of many lightning quake interpretations. Hinzen (2012) interpreted their lightning quake signal as a combination of the direct acoustic arrival, primarily visible in the vertical component of their seismogram, followed by the explosion of a lightning-struck tree. Lin and Langston (2007, 2009a,b) have done extensive work on lightning quakes. First, they found that thunder excited *P* and *S* reverberations in the near surface, and that these reverberations decayed with depth in a way consistent with the retrograde elliptical particle motion of air-coupled Rayleigh waves. The existence of a "locked-mode" Rayleigh wave rather than a "leaky-mode" wave required near-surface velocities lower than the acoustic velocity in air and also depended on the incident angle of the thunder source. This led them to conclude that acoustically induced ground motions depend primarily on the material properties of the top 30 m of the near surface, which is corroborated by earlier studies (Espinosa *et al.*, 1968; Sabatier and Raspet, 1988; Langston, 2004). In a second study, they added that the lightning quake signals were first initiated in the ground some hundreds of meters from the receiver array. They concluded that lightning quake ground motions, and possibly other airborne pressure sources, could be used to constrain substrate velocities and average layer thicknesses (Lin and Langston, 2009b).

Other recordings of atmospheric shockwave sources (bolides; bombs; artillery; missile blasts; and volcanic eruptions) also shed light on the mechanics of the coupling between acoustic and seismic waves (Espinosa *et al.*, 1968; Sabatier and Raspet, 1988; Kitov *et al.*, 1997; Garcés *et al.*, 1998; Langston, 2004; Arrowsmith *et al.*, 2010; Albert *et al.*, 2013; Solomos *et al.*, 2016; Novoselov *et al.*, 2020). Albert *et al.* (2013) and Kitov *et al.* (1997) analyzed controlled airborne explosive blasts over a variety of ground types, receiver distances, explosive altitudes, and explosive magnitudes. Both studies saw two types of acoustic-to-seismic signals: one consistent with the seismic ground velocity (the "upstream arrival" Albert *et al.*, 2013) and one matching the airborne acoustic wave velocity (the "direct arrival"). Kitov *et al.* (1997) showed that the upstream arrivals are air-coupled Rayleigh waves and are much stronger when the source is closer to ground level. Albert *et al.* (2013) posited that this arrival is coupled very near to the source and travels primarily through the ground to the receiver. The direct arrival signal is theorized to be a result of constructive interference between the incident acoustic wave and the previously ground-coupled Rayleigh wave (Kitov *et al.*, 1997). This is seen by a change in the central frequency of sources at various distances: dominant frequencies and signal lengths of the direct arrival increased with epicentral distance. This is explained by the effects of acoustic incidence and epicentral distance on apparent horizontal slowness in the coupled wavetrain. At longer distances, the apparent horizontal slowness of the incident wave approaches the true acoustic velocity. This in turn creates an acoustic-to-seismically coupled wave with a higher frequency, consistent with their observations. The dynamic characteristics of the acoustic-to-seismic signal of lightning quakes can be related to the characteristics of the source lightning channel. For example, DAS strain-rate measurements are positively correlated with lightning peak current (Zhu and Stensrud, 2019), as are vertical seismic displacement (Lin and Langston, 2009b; Novoselov *et al.*, 2022).



Downloaded from http://pubs.geoscienceworld.org/ssa/bssa/article-pdf/doi/10.1785/0120230116/5983977/bssa-2023116.1.pdf
by Pennsylvania State University user

Beyond acoustic-to-seismic ground coupling of thunder's acoustic wave, lightning presents another possible source in its powerful electromagnetic (EM) field. A lightning bolt's EM field strength can be understood through its dipole moment, which can be over 150 C km (Nieckarz *et al.*, 2011). Via a lesser known phenomenon called "electroseismic (ES)" coupling, EM fields have been shown to couple with seismic wavefields in saturated porous media, such as wet ground, and produce a variety of coupled electroseismic wave phases (Pride, 1994; Pride and Haartsen, 1996; Haartsen and Pride, 1997; Dupuis *et al.*, 2007; Zhu *et al.*, 2008; Gao *et al.*, 2017; Liu *et al.*, 2018; Potylitsyn *et al.*, 2019; Wang *et al.*, 2020; Fischer, 2021; Zheng *et al.*, 2021). Because ES coupling is not a commonly discussed phenomenon, we will recount its theory briefly here: an EM source applied to the fluid-saturated medium induces relative ground-to-fluid oscillations by pore-scale electroosmotic forces (Fischer, 2021). These relative ground-to-fluid motions, along with the EM fields, constitute the total ES wavefield. The ES wavefield is characterized by two main types of coupled waves: "coelectric" waves and "interface responses" (IRs) (Fischer, 2021). The coelectric wave is a seismic wave coupled closely into the EM wavefield, traveling at the EM velocity and with amplitudes proportional to the EM wavefield strength (Garambois and Dietrich, 2001). Because these coelectric waves move at EM velocities, they appear as signals with essentially zero seismic moveout. The second main type of coupled ES wave is the interface response, which derives its name from the method of generation: upon interacting with a subsurface interface, asymmetric electro-osmotic forces induce independently propagating seismic *P* waves, which can lead to the production of other seismic wave phases and surface waves. We term these waves as ES *P* waves and ES surface waves (Pride and Haartsen, 1996; Haartsen and Pride, 1997; White and Zhou, 2006; Slob and Mulder, 2016; Gao *et al.*, 2017; Peng *et al.*, 2018; Wang *et al.*, 2020). In summary, an EM source, such as the powerful EM dipole created by a lightning bolt, could theoretically create its own seismic wavefields. ES coupling has been thoroughly characterized by a set of governing equations that combine the Biot poroelastic equations with Maxwell's equations (Pride, 1994; Pride and Haartsen, 1996; Haartsen and Pride, 1997). The strength of the EM and ES conversion is in part controlled by the magnitude of the electric dipole moment of the source, which may be strong enough in the case of lightning to be observed at large scales. ES waves have been identified in lab settings (Zhu *et al.*, 2008; Peng *et al.*, 2018) and with active sources in the field settings (Kulessa *et al.*, 2006) but have not been observed from natural EM sources. In lab environments, it has been shown that the frequency content of an electroseismic (ES) wave matches the frequency content of an EM source (Zhu *et al.*, 2008; Peng *et al.*, 2018).

This article serves to investigate many lightning quakes measured by the Penn State DAS array. First, we investigate the role of ES-coupled wavefields in lightning quake observations. This has never yet been studied and could change how we view the generating mechanisms of lightning quakes. Beyond this, the role of acoustic-to-seismic coupling in the context of high-density DAS measurements is also unknown. We propose and demonstrate a novel data analysis technique unique to gauged DAS measurements to derive the wavefield composition. We use 3D numerical simulations of acoustic-to-seismic and ES wavefields alongside novel azimuthal strain-rate variation analysis techniques to robustly characterize the complex nature of our lightning quakes. This fusion between the atmospheric and seismic fields of the study can shed light on the source physics of natural and manmade events, the interactions between seismic waves and the atmosphere, and inversion of atmospheric and near-surface properties (Arrowsmith *et al.*, 2010).

## DATA

The data for this study were collected by the DAS cable as part of the Fiber Optic foR Environmental SEnsEing (FORESEE) project at the Pennsylvania State University, described in Zhu *et al.* (2021). The DAS array runs for 4274 m underneath the Penn State University campus, as shown in Figure 1. The DAS measurements are recorded by a Silixa iDAS2 interrogator at 500 Hz, which discretizes the cable with a 2 m channel spacing (for a total of 2137 channels) and a 10 m gauge length. The DAS system was mapped and calibrated in a previous study (Zhu and Stensrud, 2019). DAS systems are ideal for observing small-scale passive sources that occur over a wide spatial and temporal domain (Dou *et al.*, 2017; Zhu and Stensrud, 2019; Lellouch *et al.*, 2020; Walter *et al.*, 2020; Lindsey and Martin, 2021), such as lightning strikes. DAS interrogated along existing telecom cables, which are often permanent installations, continuously gather samples at high spatial densities over kilometers of cable (Dou *et al.*, 2017; Rodríguez Tribaldos and Ajo-Franklin, 2021). This dense spatial scale is further bolstered by sampling rates on the order of hundreds to thousands of Hertz. In practice, DAS instrument response is flat in phase and amplitude from 20 $\mu$Hz to signals in the kHz range (Walter *et al.*, 2020; Lindsey and Martin, 2021; Rodríguez Tribaldos and Ajo-Franklin, 2021). The fiber-optic cable used in this study, originally an unused telecommunications fiber, is laid within a concrete conduit at a generally constant depth between 1 and 1.5 m. Any excursions from this depth to avoid prior infrastructure such as steam lines, electrical conduits, and maintenance tunnels last only a few channels. Large-scale infrastructure, such as campus buildings, surround much of the array from channels 800 to the end. Before this, the channels are buried along intramural sports fields unobstructed by buildings. This difference in urbanization allows us to conveniently separate our array into two sections for later analysis: section 1 refers to the unobstructed channels 0–500, and section 2 refers to the urban channels 800–2137. The channels in between these sections,



Downloaded from http://pubs.geoscienceworld.org/ssa/bssa/article-pdf/doi/10.1785/0120230116/5983977/bssa-2023116.1.pdf
by Pennsylvania State University user

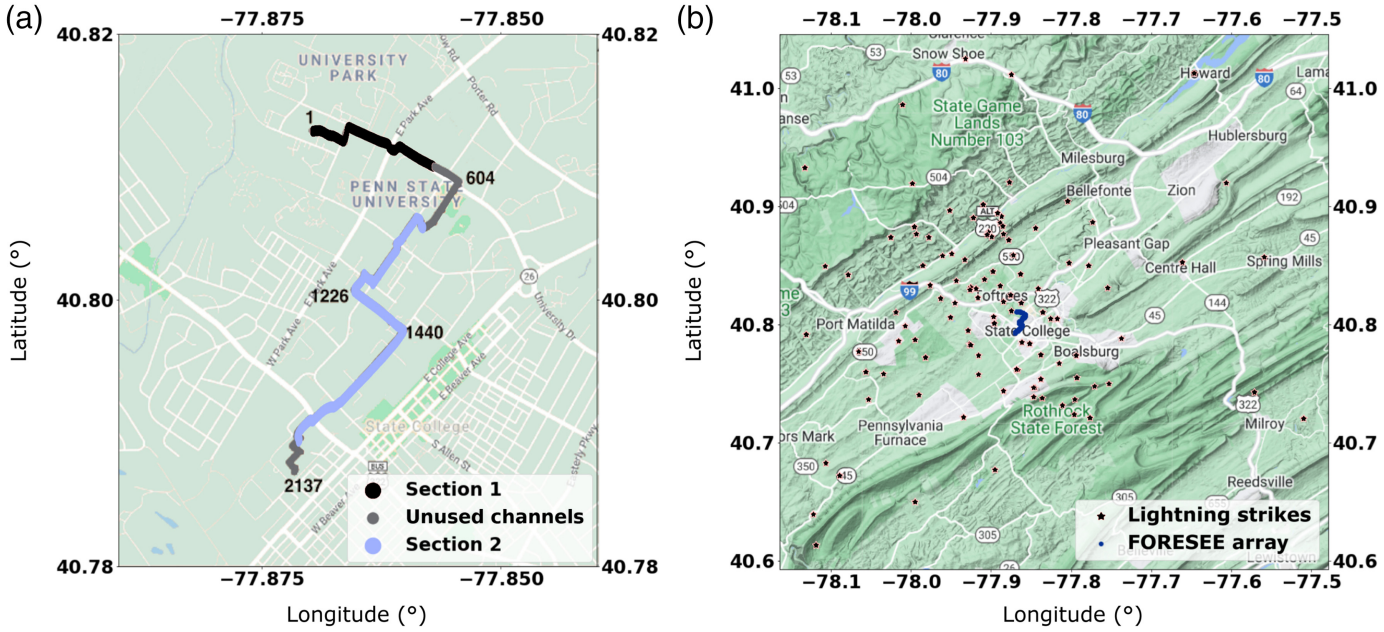



**Figure 1.** (a) Map of the Fiber Optic foR Environmental SEnsEing (FORESEE) distributed acoustic sensing (DAS) array underneath State College. (b) Map showing the location of all 109 lightning strikes used in this study, relative to the FORESEE array. The color version of this figure is available only in the electronic edition.

channels 501–799, pass beneath Penn State's athletics buildings and on-campus fields, giving it inconsistent signal quality.

The lightning quake data were collected from many storms between 5 April 2019 and 20 May 2021. In total, 458 high-fidelity lightning quake events were identified in the DAS recordings. Many of these events overlapped or were otherwise very near in arrival to other lightning quakes and were not used in this work. A previous study using FORESEE data chose a subset of 121 lightning quakes from four different thunderstorms in 2019 (Hone and Zhu, 2021). This study uses a group of 109 lightning quakes that were identified as isolated from other large signals. Each of these 109 lightning quakes, as shown in Figure 1b, is correlated to lightning events detected and reported by the NLDN. The lightning source locations are taken from NLDN records. The NLDN measures EM waves and uses the time-of-arrival approach to yield cloud-to-ground flash detection efficiencies of over 90% and location accuracy of better than 200 m (Cummins *et al.*, 1998; Nag *et al.*, 2015). The NLDN provides estimates of lightning source location and peak current used in the following analyses.

Figure 2 shows a distribution of the peak currents of lightning events in this study. Most strikes used are negatively polarized and below 50 kA in absolute peak current. The sampling distribution of all event–channel pairs is relatively even across the angle between each lightning quake source and the fiber direction at each channel (hereafter called "relative event-channel azimuth"), as shown in Figure 2b. The large sample size for event–channel pairs across all azimuths is a key benefit to using passive DAS arrays for lightning detection and analysis.

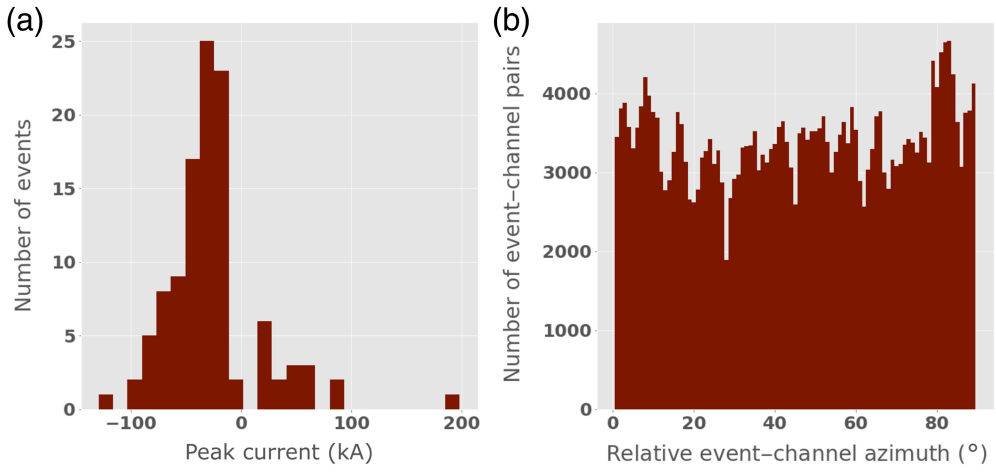



**Figure 2.** Peak current and relative event–channel azimuth distribution of the 109 events used in this study. (a) Peak current distribution. (b) Distribution of relative event–channel azimuths. The total number of counts in this distribution is equal to the combinatoric pairing of all 109 events with all 2137 DAS channels. The color version of this figure is available only in the electronic edition.



Downloaded from http://pubs.geoscienceworld.org/ssa/bssa/article-pdf/doi/10.1785/0120230116/5983977/bssa-2023116.1.pdf
by Pennsylvania State University user

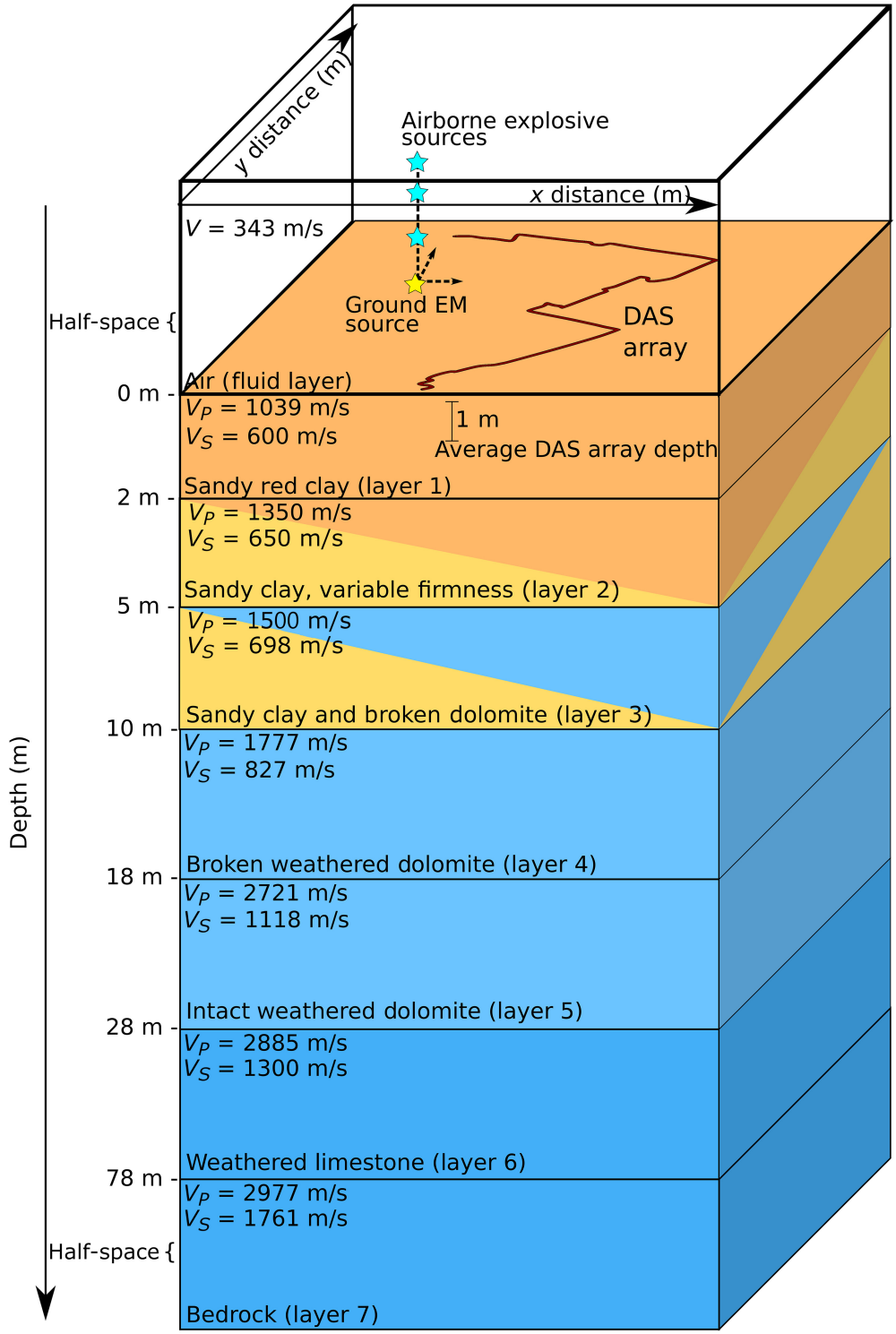



**Figure 3.** An air half-space sits over a geologic model of horizontal layers. Beneath a thin topsoil, the local geology consists of several meters of sandy red clay over unconsolidated karsty dolomite, which transitions to limestone bedrock. The deep bedrock is consolidated limestone. The geology and layer velocities are based on MASW and resistivity surveys carried out around channel 1900 for construction purposes. The yellow star represents the vertical electric dipole source placed at $z = 0$ m (Dwyer and Uman, 2014). The blue stars represent airborne explosive sources placed at various altitudes in the air layer. The color version of this figure is available only in the electronic edition.

## NUMERICAL MODELING

As an initial analysis of the lightning quakes detected by our DAS array, we utilized numerical simulation of acoustic-to-seismic and ES wavefields to qualitatively recreate two observed events. The goals of the numerical modeling were several fold: first was to discern the effects, if any, of ES-coupled waves in the lightning quake observations. The modeling would also allow us to understand the relative amplitudes of the acoustic-to-seismic waves.

### Model details

The two chosen lightning quakes were qualitatively replicated using a 3-D simulation coupling acoustic, EM, and seismic wavefields via the equations presented in Pride (1994), Pride and Haartsen (1996), Haartsen and Pride (1997), and the numerical implementation described in Gao *et al.* (2017) and Wang *et al.* (2020). The model for poroelastic and EM coupling is applied to a horizontally stratified layer model with geologic characteristics based on local multichannel analysis of surface waves (MASW) surveys (Hone and Zhu, unpublished manuscript, 2023) and ambient noise surface-wave analysis in this area (Czarny and Zhu, 2022). Figure 3 illustrates the model's layer setup, consisting of stacked horizontal layers of air, unconsolidated soils, dolomite, limestone, and bedrock. The layer properties not shown in the figure are listed in Table 1. The simulation measures the radial and transverse seismic wavefields as well as the vertical and horizontal electric and magnetic wavefields at 2137 receivers located analogously to the FORESEE DAS



Downloaded from http://pubs.geoscienceworld.org/ssa/bssa/article-pdf/doi/10.1785/0120230116/5983977/bssa-2023116.1.pdf
by Pennsylvania State University user

TABLE 1
**Parameters for the Stratified Layer Model**

| Parameter | Symbol | Porous Layers |
|---|---|---|
| Porosity | $\phi$ | 0.43 (soils) and 0.03 (other) |
| Permeability | $\kappa_0$ ($\times 10^{-12}$ m$^2$) | 10 |
| Tortuosity | $\alpha_\infty$ | 3.36 |
| Solid grain bulk modulus | $K_s$ (GPa) | 35.7 |
| Frame bulk modulus | $K_b$ (GPa) | 15 |
| Shear modulus | $G$ (GPa) | 14.7 |
| Fluid bulk modulus | $Kf$ (GPa) | 2.25 |
| Solid grain density | $\rho_s$ (kg m$^{-3}$) | 2650 |
| Fluid density | $\rho_f$ (kg m$^{-3}$) | 1000 |
| Magnetic permeability | $\mu$ (H\m) | $4\pi \times 10^{-7}$ |
| Solid relative permittivity | $\epsilon_s$ | 4 |
| Salinity of the pore fluid | $C_{f0}$ (mol L$^{-1}$) | 0.1 |
| Fluid relative permittivity | $\epsilon_r$ | 77 |
| Effective permittivity of the porous medium | $\epsilon$ ($\times 10^{-11}$ Fm$^{-1}$) | 7.2 |
| Fluid viscosity | $\eta$ (Pa · s) | 0.002 |
| Zeta potential | $\zeta$ (mV) | −17.8 |
| Rock conductivity | $\sigma_0$ (Sm$^{-1}$) | 0.06 |
| Static electrokinetic coupling coefficient | $L_0$ ($\times 10^{-10}$sCkg$^{-1}$) | 6.85 |

channels, as shown in Figure 1. The lightning source is modeled as one or more sequential airborne spherical explosions and ground-level EM dipoles. The airborne explosions represent the string-of-pearls thunder shockwaves, and an EM dipole represents the possible origin of ES waves. The lightning dipole is placed on the ground surface in accordance with the findings of Nucci *et al.* (1990) and Shoory *et al.* (2011), which state that lightning channel current and electric field are strongest at the channel base and exponentially decay with height. The lightning dipole strength is derived from the results of Nieckarz *et al.* (2011), in which cloud-to-ground lightning flashes studied through EM radiation in multiple frequency ranges were shown to have lightning dipole moments linearly correlated with their peak currents ($p \approx 7.5$I). Here, $p$ is the dipole strength and $I$ is the lightning peak current. This relation is used to approximate realistic lightning dipole strength in the model, though the amplitudes are still taken as primarily qualitative.

The blast magnitudes of thunder waves are not well studied in seismic contexts, though thunder blast overpressures have been investigated for their role in lightning-strike injuries (Blumenthal, 2016). For example, a 30 kA channel can create overpressure reaching up to 588 psi less than a centimeter from the channel's core, with the overpressure decaying with the inverse of distance (Blumenthal, 2016). Therefore, the simulated wavefield amplitudes are meant as qualitative references for the kinematics and electrokinematics of lightning quakes.

## Simulation results

Two lightning quakes were chosen for numerical simulation: events 16333 and 26059, shown alongside their synthetic simulations in Figures 4 and 5, respectively. These events were chosen due to their high signal-to-noise ratio (SNR) and contrasting features. Figure 4c shows the strain-rate data for event 16333, which occurred on 7 July 2021, 2 km from the center of the FORESEE array. The event had an estimated peak current of −20 kA. This event lacks the characteristic repetitions of event 26059, instead being composed of a single powerful arrival. The ES-wave arrivals (ES *P* wave and ES surface waves) of an EM source at the base of the lightning channel do not match the observed lightning quake. A single airborne explosive source, seen in Figure 4b, qualitatively recreates event 16333 best. Despite the qualitative alignment, significant differences in the simulated signal and observed earthquake should be noted. The observed lightning quake shows a drawn-out signal with several "pulses," in which the simulated explosive source is a single, short signal. The source complexity of lightning is certainly a factor in this difference. In a more realistic model, lightning bolts, by the nature of their underlying physics, are sources of tortuous geometry. This tortuosity can create branches and twists, or the bolt can curve into the clouds and stretch for many kilometers. Along the length of the bolt, thunder may vary in source power due to severe temperature nonuniformities. Beyond its inception, the propagation of thunder is also complex. Thunder refracts through the nonuniform atmosphere, oftentimes bending upward due to temperature-based refraction before arcing back down toward the ground. These source and propagation complexities could conceivably greatly affect the character of the observed lightning quake signal.

Figure 5c shows the DAS strain-rate data for event 26059. This event occurred on 10 June 2020, less than a kilometer to the southwest of the end of the FORESEE array. The event had an estimated peak current of −33 kA. This event shows repetitions similar to reflections or repeated lightning strokes. However, the timing of these repetitions is orders of magnitude too long for typical repeated lightning strokes and also too long for conceivable cloud-induced or subsurface-induced reflections. We believe that these repetitions are evidence of the string-of-pearls shockwave induction theory (Few, 1969), combined with the effects of local temperature increases along the lightning bolt's length, which in turn cause additional thunder shockwaves from the same lightning bolt. These individual thunder shockwaves, if distributed along the multiple-kilometer-long lightning bolt, would have arrival times consistent with the repetitions we see in event 26059. Figure 5b shows the model of this lightning quake using a string of explosive sources at altitudes of 360, 560, 800, 940, 1080, 1220, and 1360 m. Figure 5a shows the simulation for only a single EM source at the base of the lightning channel, which shows the characteristic direct coelectric wave and electroseismically induced surface waves. The string-of-pearls airborne explosive sources qualitatively match the observation much more than the EM source.



Downloaded from http://pubs.geoscienceworld.org/ssa/bssa/article-pdf/doi/10.1785/0120230116/5983977/bssa-2023116.1.pdf
by Pennsylvania State University user

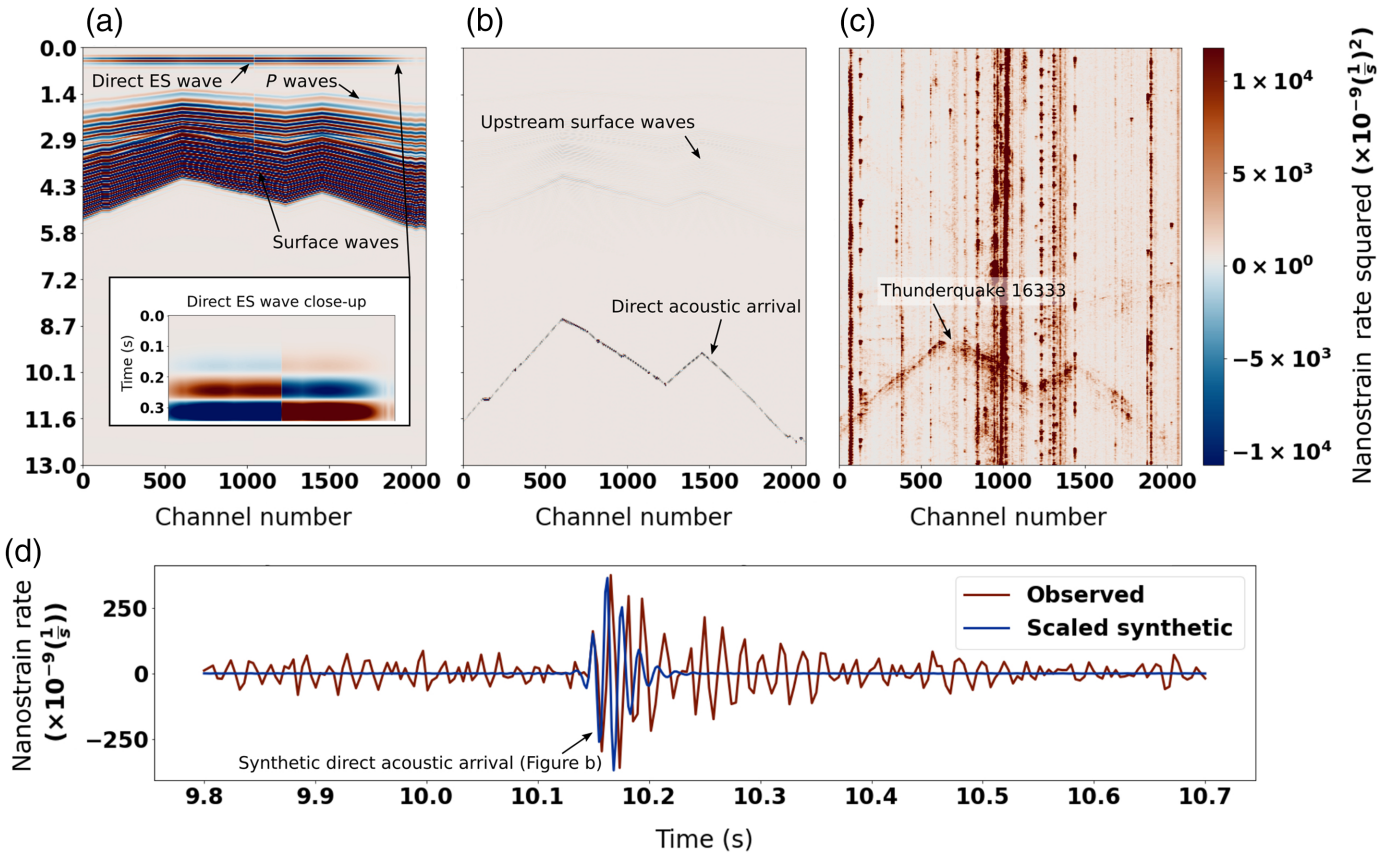



**Figure 4.** Simulation results for event 16333. (a) Results for an electromagnetic (EM) source placed at the base of the event 16333 lightning channel. The inset shows a close-up view of the first 0.3 s of this simulations, in which the direct ES waves reached the receivers. The later ES arrivals and ES surface waves can also be seen. The ES surface waves are already highly dispersed by the time they reach the receivers. (b) The results for a single airborne explosive source. (c) The DAS observation of this event. The raw strain-rate data are squared to improve the visibility of the event. (d) A single trace from channel 800 overlaid from the airborne explosive simulation and the observed event. The color version of this figure is available only in the electronic edition.

The EM sources for both lightning quakes (Figs. 4a and 5a) show significant direct coelectric waves of magnitudes comparable with the surface waves produced by an ES conversion at the air–ground interface. These direct coelectric signals are not seen in the data. This suggests that electroseismically converted waves do not play a significant role in the lightning quake signals at these distances. This does not discount the possibility of electromagnetically induced seismic waves from lightning bolts entirely, however. Although an EM field created by lightning is powerful, on the order of 100 million volts (Dwyer and Uman, 2014), the short duration of the field pulse would theoretically couple into an extremely high-frequency ES wave on the order of 1000 Hz (Peng *et al.*, 2018). This high-frequency wave might attenuate quickly in the near surface and become invisible to our underground sensors within a matter of meters from the lightning channel. The simulations shown in Figures 4 and 5 are shortcoming in their frequency content, considering only an EM dipole pulse at seismic frequencies. The code utilized in this study was not able to implement dipole sources of high realistic frequency; thus, we are not able to capture the full physics of lightning's ability to induce ES waves. The simulations do show that if a lightning quake was created by a powerful, low-frequency dipole source, the direct coelectric arrival would be equal to or greater than the ES surface waves in amplitude.

The numerical simulations show that airborne explosions are the major contributing source in lightning quakes. The signal arrivals match the travel time expected for acoustic waves coupled near the channels. The observed signals are more complicated than the effects captured in the model used, thus requiring a data-driven dynamical approach to more fully understand the effects of acoustic seismic coupling on the lightning quake wavefield. In addition, because of the difficulty in estimating lightning bolt explosive "magnitude," these simulation results are only qualitative.

## WAVEFIELD ANALYSIS

### Azimuthal sensitivity method

Although the numerical modeling showed that the lightning quakes we observed match the expected travel time of acoustic waves, the nature of the wavefield during and after the acoustic-to-seismic coupling remains poorly understood. A data-



Downloaded from http://pubs.geoscienceworld.org/ssa/bssa/article-pdf/doi/10.1785/0120230116/5983977/bssa-2023116.1.pdf
by Pennsylvania State University user

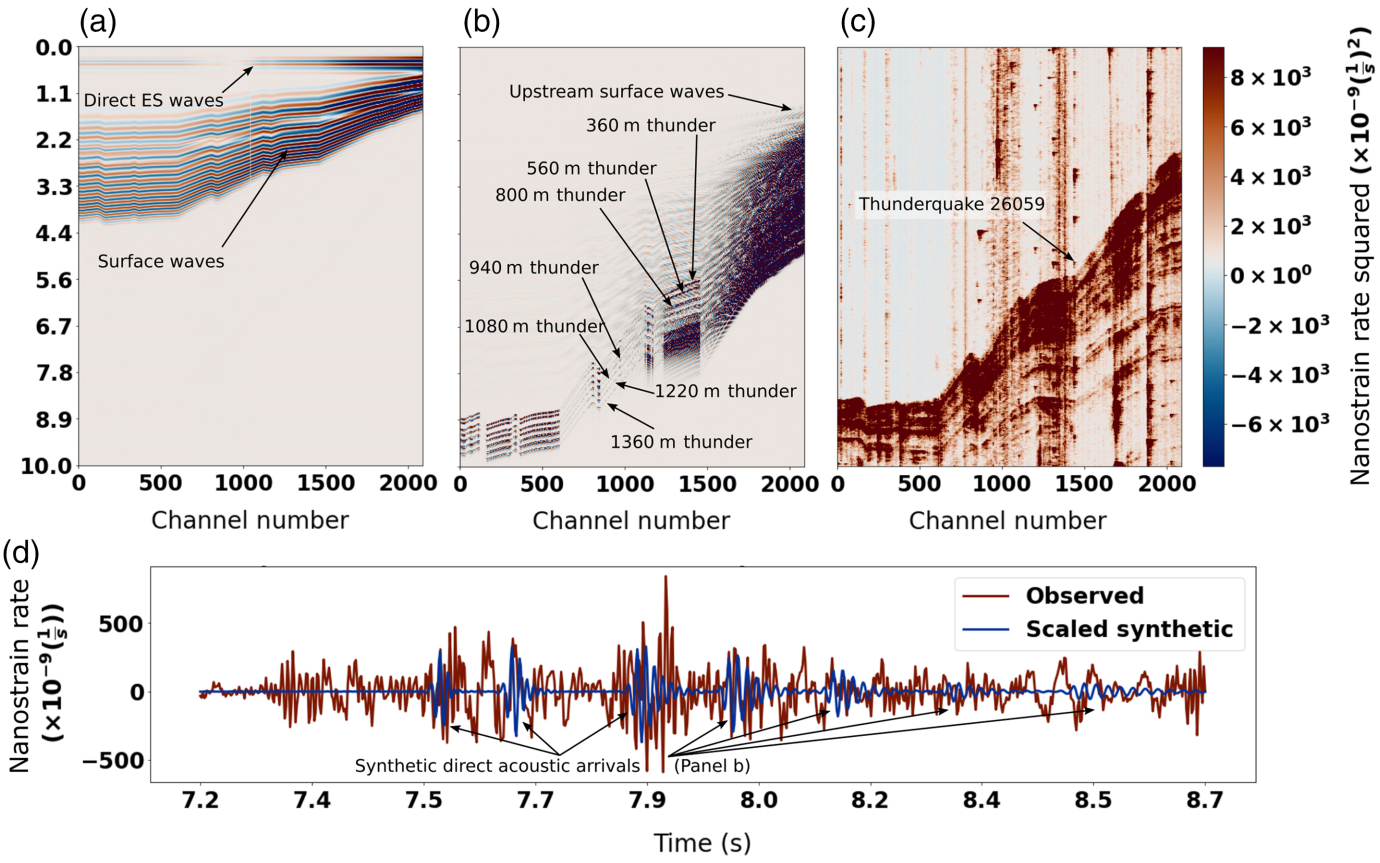



**Figure 5.** Simulation results for the event 26059. (a) Results for an EM source placed at the base of the event 26059 lightning channel. (b) The results for seven stacked airborne explosive sources. Multiple sources were used for this event to demonstrate the ability of the "string-of-pearls" model to reproduce the observed lightning quake. (c) The DAS observation of this event. The raw strain-rate data are squared to improve the visibility of the event. (d) A single trace from channel 800 overlaid from the airborne explosive simulation and the observed event. The color version of this figure is available only in the electronic edition.

driven approach was taken to further understand the nature of the acoustic-to-seismic coupling and the wave types observed by the FORESEE DAS array. The method pursued here is novel and takes advantage of the intrinsic azimuthal sensitivity of DAS array strain-rate measurements as well as the large data set provided by the FORESEE DAS array and the clear lightning quake events. DAS arrays collecting data over a certain gauge length have inherently different measurement sensitivities depending on the relative angle between the source and the fiber direction (Martin *et al.*, 2021). The definition of "sensitivity" used here was introduced in Martin *et al.* (2021). In brief, the sensitivity is the predicted strain-rate measurement of a particular wave (Martin *et al.*, 2021). By comparing the relative event–channel azimuth with the measured DAS strain rates, it is possible to independently determine dominant wave types, subsurface-wave velocities, and fiber depth in the absence of other, more traditional, techniques. Because this method has not been used before in any known published work, it will be greatly elucidated here.

The 109 chosen events were first band passed between 20 and 120 Hz. Next, the maximum three strain rates were picked and averaged at each of the 1800 channels in sections 1 and 2 for each of the 109 events, giving a total of ~166,000 strain rates. Given source coordinates provided by the NLDN, acoustic travel-time estimates were used to generate narrow time windows for these strain-rate picks. Examples of these picking windows are shown in Figure 6. The lightning bolt peak current and relative source–channel azimuth were tracked for each of these 166,000 strain rates. These measurements were normalized for the linear effects of peak current (shown by Novoselov *et al.*, 2022) by dividing the strain-rate values by the peak currents of their corresponding lightning bolts. Subsequently, the attenuating effects of event–channel distance were accounted for. Equation (1), the attenuation function for acoustic waves presented by Langston (2004), was fit to the 166,000 strain rates using a standard linear regression method, as shown in Figure 7. The fit was divided out of the strain rates, normalizing the effects of event distance,

$$A(r) = \frac{A_0}{r^n}\exp\left(-\frac{fr}{4\pi v_{\text{air}}Q}\right), \tag{1}$$

in which, $A(r)$ is the amplitude as a function of distance; $A_0$ is the amplitude at the source; $r$ is the distance; and $n$ is the



Downloaded from http://pubs.geoscienceworld.org/ssa/bssa/article-pdf/doi/10.1785/0120230116/5983977/bssa-2023116.1.pdf
by Pennsylvania State University user

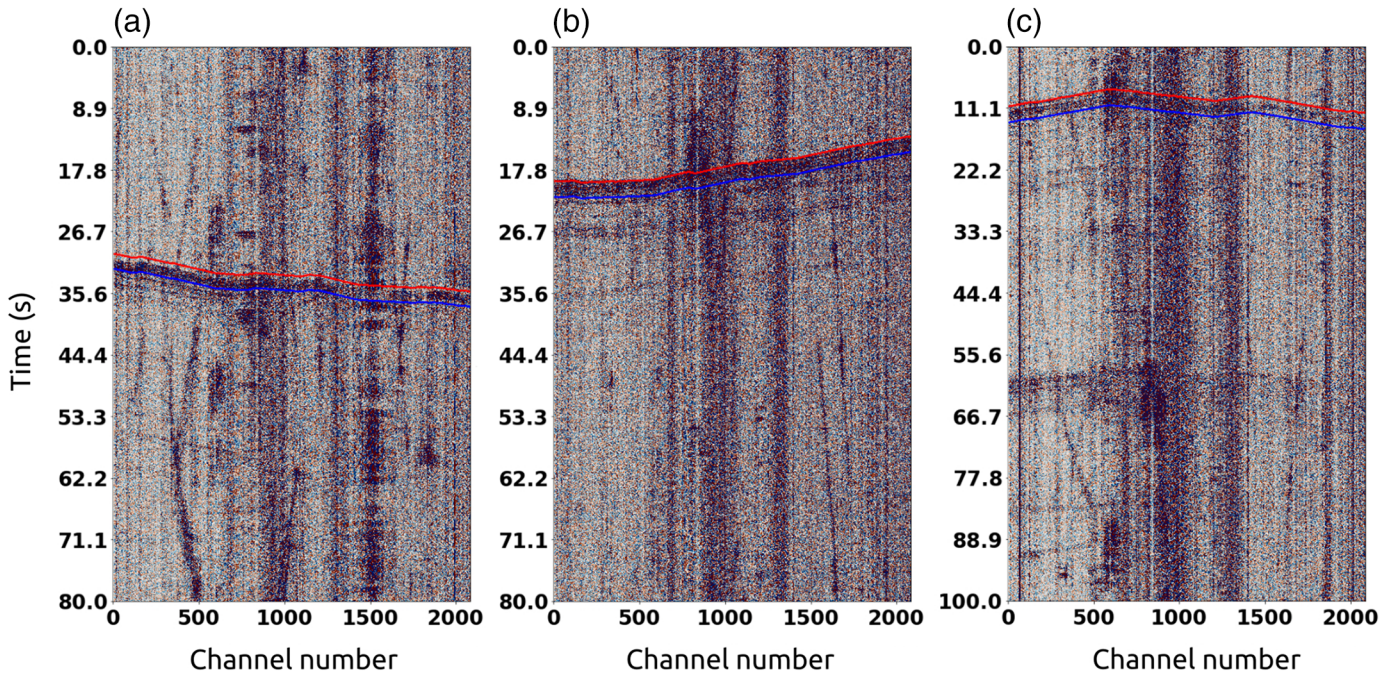



**Figure 6.** Examples of raw lightning quake recordings and the picking windows used for the azimuthal strain-rate variation analysis and frequency analysis. The picking windows are bounded by the red and blue lines on each figure. The time axis on each recording is zeroed based on an automated data slicing algorithm and does not represent any absolute time. (a) Event 23408. (b) Event 384. (c) Event 16585. The color version of this figure is available only in the electronic edition.

geometrical spreading factor (1 for spherical point sources in the atmosphere, as Farges and Blanc, 2010); $Q$ is the frequency-dependent quality factor (representing physical atmospheric absorption of energy and atmospheric scattering effects); $f$ is the frequency; and $v_{air}$ is the acoustic velocity in the air (taken as 343 m/s).

With peak current and distance effects removed, the resulting normalized strain rates were analyzed as a function of relative event–channel azimuth. For each section, Markov chain Monte Carlo (MCMC) simulations were used to fit the data to azimuthal sensitivity equations derived by Martin *et al.* (2021). For both sections, two assumed wavefield cases were considered, hereafter referred to as "case 1" and "case 2": case 1 assumes only direct acoustic-to-seismic coupling of the thunder pressure wave, with no secondary sources. Case 2 includes the possibility of secondary sources excited by the incident acoustic wave. These choices in speculated wavefield character and the sensitivity functions included in both cases are discussed here. A DAS cable installed in an empty region with absolutely no nearby infrastructure or topography would expect a wavefield consisting of only air-coupled *P–SV* waves. The nature of the air-coupled *P–SV* waves will depend on the relative apparent slownesses of the air and the ground, along with the angle of incidence of the acoustic wave (Kennett, 2023). According to the analysis of Kennett (2023), a fundamental mode of the Rayleigh wave is expected to appear in all the situations. Thus, the DAS sensitivity to the Rayleigh wave is included in both test cases. It is important to disclaim, though, that this theory is controversial. A more general understanding of the air-coupled *P–SV* case could be the production of surface-confined *P* and *SV* waves with Rayleigh-like particle motion. Case 1 tests this simplified wavefield assumption in which the Rayleigh wave is the only component of the wavefield. The path of the FORESEE fiber-optic cable is not installed within such an empty region, however, and a more complex wavefield might be expected. The acoustic thunder wave could interact with local topography, fences, buildings, the edges of sidewalks, signs and other posts, or trees. Such interactions could produce local wave energy that could be

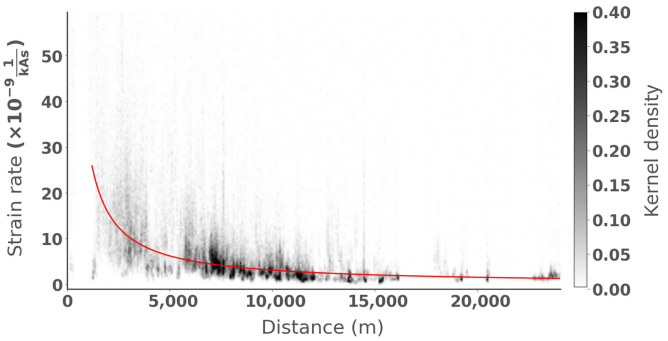



**Figure 7.** All strain-rate picks plotted as a point kernel density as a function of distance ($n$ = 166,231). The strain rates are normalized by the peak current of their corresponding lightning bolts. The plotted line is the regression fit to equation (1). The color version of this figure is available only in the electronic edition.



Downloaded from http://pubs.geoscienceworld.org/ssa/bssa/article-pdf/doi/10.1785/0120230116/5983977/bssa-2023116.1.pdf
by Pennsylvania State University user

transverse to the assumed direction of propagation, which is defined by the relative source–channel azimuth used in the analysis. Because the largest transverse energy typically comes from Love waves, we include the DAS sensitivity to Love waves in case 2. In summary, the data are fit to the Rayleigh-wave sensitivity equation in case 1, then to the weighted sum of the Rayleigh and Love sensitivity equations in case 2. In this way, we test for the presence of wave energy generated by local sources. In both cases, the equations are integrated over 20 to 120 Hz. At each frequency step, the expected sensitivity equations were scaled by that frequency's spectral power in the data.

The Rayleigh and Love sensitivities follow the equations here:

$$\dot{\sigma}_{g,z,R} = \frac{2c_R k}{g}\cos(\phi)\sin\left(\frac{kg * \cos(-\phi)}{2}\right)(A_R e^{-\gamma_\alpha kz} + iB_R\gamma_\beta e^{-\gamma_\beta kz}), \quad (2)$$

$$\dot{\sigma}_{g,z,L} = -\frac{2c_L k}{g}\sin(\phi)\sin\left(\frac{kg * \cos(\phi)}{2}\right)(A_L e^{-i\eta_1 kz} + B_L e^{i\eta_1 kz}), \quad (3)$$

in which $\dot{\sigma}_{g,R}$,$\dot{\sigma}_{g,L}$ are the expected pointwise axial strain-rate measurements for Rayleigh and Love waves, respectively, averaged over the fiber gauge length $g$ at depth $z$; the relative event–channel azimuth is shown as $\varphi$ and the wave frequency band is $f$; variables $c_R$,$c_L$ are the phase velocities of Rayleigh and Love waves in the medium, respectively, and $k = \frac{f}{2\pi c}$ is the wavenumber. Love-wave group velocity in the surface layer $\beta_1$ is set to a typical $0.9c_L$; Rayleigh irrotational component velocity $\alpha$ is set to $1.03c_R$; Rayleigh solenoidal component velocity $\beta$ is set to $c_R$. The equations are simplified with the definitions $\gamma_\alpha = \sqrt{1-\frac{c_R^2}{\alpha^2}}$, $\gamma_\beta = \sqrt{1-\frac{c_R^2}{\beta^2}}$, and $\eta_1 = \sqrt{\frac{c_L^2}{\beta_1^2}-1}$. Finally, $A_R$,$B_R$ are empirical Rayleigh amplitude factors the ratio for which is related to the wave ellipticity, and $A_L$,$B_L$ are empirical amplitude terms of the depth factor for Love waves. The full derivation of these equations is presented in Martin *et al.* (2021). These equations show that the expected strain-rate measurements of a gauged DAS array are strongly modulated by relative event–channel azimuth, wave velocity, wavefield frequency band, and fiber depth, among other parameters.

The strain-rate picking method used in this analysis, which focused on the largest amplitudes visible in the time-domain channel traces, would naturally be biased toward the compounded strain rates. Thus, case 2, the weighted sum of the equations was used. The weights themselves, denoted as $W_{R,L}$ for each wave type, respectively, were also solved for using the MCMC. In case 1, because only the Rayleigh equation was fit, the weight $W_R$ was fixed to unity. The gauge length is derived from our general FORESEE DAS array configuration. Because DAS sensitivity is rotationally symmetrical, the relative event–channel azimuth $\varphi$ is collapsed from 360° to a range of 90°. The MCMC was run for 11 million steps, well beyond convergence, and the resulting chains were thinned to mitigate autocorrelation.

The maximum-likelihood parameter sets cases 1 and 2 were picked from the chains and fit to the data of sections 1 and 2, as shown in Figure 8. The maximum log likelihoods for each case and section are as follows, in which a value closer to zero is considered a better fit: case 1, section 1: −33.8; case 2, section 1: −2.4; case 1, section 2: −24.4; and case 2, section 2: −5.8. Based on these maximum log likelihoods, case 2, the weighted sum of the Rayleigh and Love waves was chosen as the better fit for both sections and given additional focus here. The nonvarying parameters of equations (2) and (3) for the case 2 fits are shown in Table 2, and the maximum-likelihood results of the variable parameters are shown in Table 3. The statistics around the maximum-likelihood parameter set for case 2 are shown in Table 4.

Focusing in on the maximum-likelihood parameter set of the Rayleigh and Love case, the main differences for sections 1 and 2 lie in the relative strengths of the empirical amplitude factors $A$ and $B$, as well as a notable shift in Rayleigh phase velocity in the urban section 2. The amplitude factors shift from being slightly Love dominant ($A_L$,$B_L > A_R$,$B_R$) in section 1 to being more balanced (with a notable drop in the Love depth factor, $B_L$) in section 2. In addition, the urban section 2 also sees a shift toward lower Rayleigh-wave phase velocities of $c_R \approx 260$ ms$^{-1}$ from $c_R \approx 340$ ms$^{-1}$ in section 1. This urban Rayleigh phase velocity is corroborated by results from recent hammer-strike tests carried out along the FORESEE array on campus, which derive a shallow Rayleigh phase velocity of $c_R \approx 250$ ms$^{-1}$ from dispersion analysis (Czarny, unpublished manuscript, 2023). The differences in empirical amplitude factors and Rayleigh phase velocity could be due to changes in near-surface geology, fiber coupling, or subsurface infrastructure. The results demonstrate that fitting the normalized strain rates as a function of relative event–channel azimuth allows the derivation of average Rayleigh and Love phase-wave velocities in the subsurface layer housing the DAS fiber.

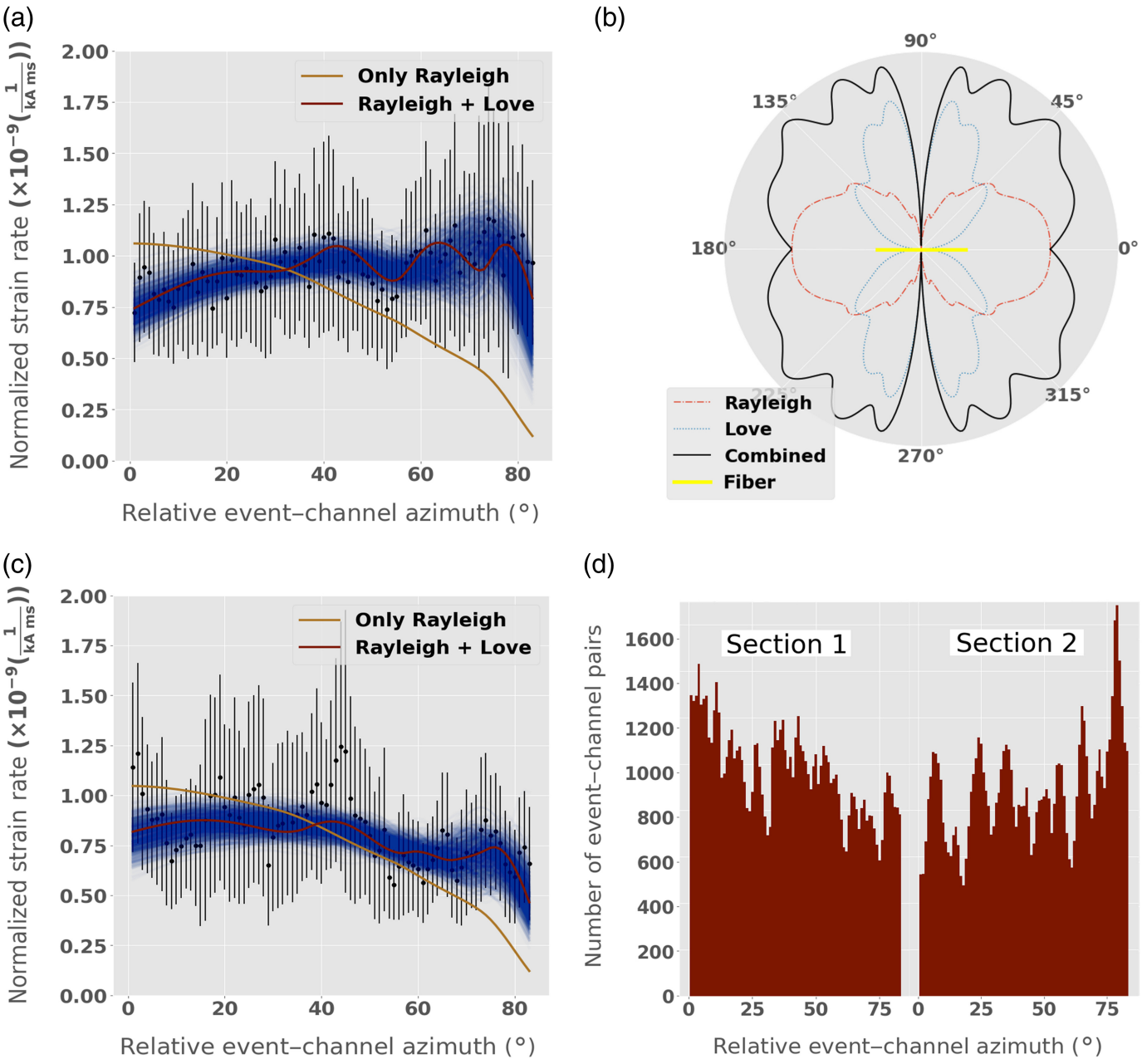
Infrastructure seems to play an important role in the normalized strain rates, seen by the differences between sections 1 and 2 in Figure 8. Mean normalized strain rates from section 1 of the array show less overall scatter, especially in the lower relative event–channel azimuths. The differences in sections 1 and 2 are further investigated through lightning quake power spectral densities (PSDs) in the next section.

## Frequency content

An analysis of lightning quake PSDs in fiber sections 1 and 2 provides additional evidence for the effects of urban areas on acoustic-seismic coupled waves. Median PSDs are shown in Figure 9. The PSDs were calculated from the same time windows used for strain-rate picks exemplified in Figure 6, then smoothed with a Gaussian kernel, averaged, and normalized by their



Downloaded from http://pubs.geoscienceworld.org/ssa/bssa/article-pdf/doi/10.1785/0120230116/5983977/bssa-2023116.1.pdf
by Pennsylvania State University user




maximum value. The raw DAS signal was not bandpassed before calculating the PSDs because it was for the azimuthal variation analysis. A significant shift in frequency power content is seen between open and urban fiber sections. The changes in frequency content cannot be pinned to one certain cause; however, several possibilities may contribute to the shift. First, scattering from urban infrastructure could attenuate certain frequencies. The thunder travels through the air at approximately the speed of sound, 343 $ms^{-1}$, with wavelengths of around 3–20 m. At these wavelengths, trees, houses, or academic buildings could realistically scatter and attenuate incoming waves of certain frequencies. A second possibility is one illuminated by the DAS sensitivity fit to the normalized strain rates in section 2 of the fiber. Because of the subterranean urban infrastructure, higher frequencies might be preferentially attenuated.

**Figure 8.** (a,c) Each data point represents the median normalized strain rate at the given relative event–channel azimuths. Error bars are the median absolute deviation of the median over all the measurements for a given azimuth. The red central fit lines show the maximum-likelihood solutions for case 2, which includes the weighted sum of equations (2) and (3). About 1500 other Markov chain Monte Carlo (MCMC) parameter sets from case 2 are shown behind the central fit to show the variation in the MCMC results. The orange line sloping downward toward higher azimuths is the fit of the maximum-likelihood parameter set of case 1. (a) Strain rates from section 1 of the FORESEE array. (c) Strain rates from section 2. (b) The full solution to equations (2) and (3) and their sum for case 2, section 1. The rotational symmetry of DAS sensitivity is easily seen here. (d) The number of lightning quake event–channel pairs used in panels (a and c). Each bar in the sampling distribution corresponds to the same strain-rate data point of the same relative event–channel azimuth in panels (a and c). The color version of this figure is available only in the electronic edition.



Downloaded from http://pubs.geoscienceworld.org/ssa/bssa/article-pdf/doi/10.1785/0120230116/5983977/bssa-2023116.1.pdf
by Pennsylvania State University user

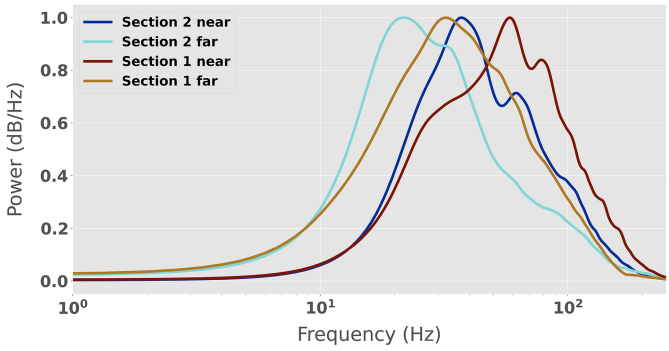



**Figure 9.** Mean frequency content of all nearby and distant lightning quakes from both sections 1 and 2. Nearby lightning quakes are defined as occurring less than 2500 m from any fiber-optic channel in the relevant fiber section. Distant lightning quakes are defined as occurring over 15,000 m from any channel in the section. The color version of this figure is available only in the electronic edition.

TABLE 2
**Given Parameters for the Distributed Acoustic Sensing (DAS) Sensitivity Equations**

| Parameter | Description | Value |
|---|---|---|
| $\phi$ | Relative event–channel azimuth | 0°–90° |
| $f$ | Frequency band | 20–120 Hz |
| $g$ | Gauge length | 10 m |

## DISCUSSION AND CONCLUSION

This study utilizes both numerical modeling and wavefield analysis to explore the nature of lightning quake wavefields detected using the FORESEE DAS array. The numerical simulations of lightning quakes 26059 and 16333 show that electroseismic coupled seismic waves are not present in the observed lightning quakes. The implications of this finding are that lightning quake observations are primarily caused by acoustic waves, which travel through the air almost the entire distance between the event source and the DAS channel. The added complexity of electroseismic coupling does not need to be considered when doing more in-depth data analysis, as was done here. Two speculated wavefield cases were fit to normalized strain-rate measurements: case 1, considering only Rayleigh energy, and case 2, considering both Rayleigh and Love energy. Case 2 fit far better, implying that both air-coupled Rayleigh waves and locally sourced Love-wave components were required to fit the data. Case 1, including only Rayleigh waves, fit the data poorly. Surface-wave phase velocities averaged in the frequency band of 20–120 Hz were extracted from the lightning quake signals using azimuthal variations in normalized strain-rate measurements. The inclusion of local Love wave, or more generally locally sourced wave-motion transverse to the assumed direction of propagation, is a unique finding in the study of lightning quakes and DAS. This has implications for future analysis of lightning

TABLE 3
**Maximum-Likelihood Parameters for the Distributed Acoustic Sensing (DAS) Sensitivity Equations Used in Case 2**

| | | Maximum-Likelihood Value | |
|---|---|---|---|
| **Parameter** | **Description** | **Section 1** | **Section 2** |
| $c_R$ | Rayleigh phase velocity | 336 $ms^{-1}$ | 260 $ms^{-1}$ |
| $c_L$ | Love phase velocity | 363 $ms^{-1}$ | 372 $ms^{-1}$ |
| $A_R$ | Rayleigh amplitude term | $8 \times 10^{-5}$ | $1 \times 10^{-4}$ |
| $B_R$ | Rayleigh amplitude term | $8 \times 10^{-5}$ | $1 \times 10^{-4}$ |
| $A_L$ | Love amplitude term of depth factor | $2.2 \times 10^{-4}$ | $1 \times 10^{-4}$ |
| $B_L$ | Love amplitude term of depth factor | $1.8 \times 10^{-4}$ | $3 \times 10^{-7}$ |
| $z$ | Fiber depth | 1.9 m | 1.7 m |
| $W_R$ | Rayleigh weight | 0.60 | 0.60 |
| $W_L$ | Love weight | 0.60 | 0.62 |

TABLE 4
**Variation Statistics for the Core Distributed Acoustic Sensing (DAS) Sensitivity Results of Case 2**

| | | Median, First and Third Quantiles | |
|---|---|---|---|
| **Parameter** | **Description** | **Section 1** | **Section 2** |
| $c_R$ | Rayleigh phase velocity | $249^{127}_{-101}$ $ms^{-1}$ | $239^{108}_{-107}$ $ms^{-1}$ |
| $c_L$ | Love phase velocity | $465^{130}_{-134}$ $ms^{-1}$ | $384^{77}_{-74}$ $ms^{-1}$ |
| $Z$ | Fiber depth | $1.0^{0.7}_{-0.7}$ m | $0.8^{0.5}_{-0.8}$ m |
| $W_R$ | Rayleigh weight | $0.6^{0.3}_{-0.3}$ | $0.5^{0.4}_{-0.3}$ |
| $W_L$ | Love weight | $0.5^{0.3}_{-0.3}$ | $0.4^{0.3}_{-0.2}$ |



Downloaded from http://pubs.geoscienceworld.org/ssa/bssa/article-pdf/doi/10.1785/0120230116/5983977/bssa-2023116.1.pdf
by Pennsylvania State University user

quakes with DAS systems: local infrastructure, such as buildings, trees, light poles, fences, and topography should be considered in the analysis of lightning quake wavefields.

Because of the differences between the results from sections 1 and 2 of the DAS fiber, it is clear that infrastructure has a large effect on the scatter of normalized strain-rate measurements and lightning quake frequency content. Unobstructed channels in section 1 show a tighter trend in their mean normalized strain rates. Uncertainty in the measured strain rates may be due to variable fiber coupling or local channel geology. The FORESEE array is a repurposed telecommunications fiber, so coupling quality is unknown along the length of the array. These same uncertainties are surely present in the mean normalized strain rates of section 2 as well. Beyond these, additional scattering is seen in the strain rates of lightning quakes impinging on the fiber at low-relative event–channel azimuth in section 2, from ~20° to 0°. One possible phenomenon contributing to this observed scatter is specular and diffuse reflection along the road corridors. The majority of the section 2 channels run along university streets flanked on either side by academic buildings, such that thunder at low-relative event–channel azimuth would propagate along the road corridor. A study by Onaga and Rindel (2007) shows that acoustic energy along urban streets is subject to significant specular and diffuse reflections due to building facades and street surfaces. Roadside building reflection could change the apparent azimuth of the acoustic wave relative to the fiber-optic cable to one of the greater sensitivity. This would result in the artificial inflation (or reduction, depending on the new azimuth) of the mean normalized strain rates plotted in the low-relative event–channel azimuths in Figure 8.

This is the first study to use an azimuthal axial strain rate variation technique with a DAS array to investigate acoustic-to-seismic coupling of atmospheric sources. The field of DAS is quickly improving, and new advancements could greatly develop this method. Future studies utilizing three-component DAS with helically wound fiber could investigate the effects of azimuthal sensitivity in multiple components. Further study on lightning quake source geometry and acoustic propagation may be able to determine the exact distance of the acoustic-to-seismic coupling, which could more easily allow lightning quakes to act analogously to locally induced seismic sources for subsurface exploration. A pioneering study by Lin and Langston (2009a) used a seismometer–microphone dual recording of thunder to estimate substrate velocities and the average thickness and velocities of near-surface layers. Hone and Zhu (unpublished manuscript, 2023) compared shear-wave profiles obtained through dispersion analysis of lightning quakes with the profiles obtained from active-source MASW analysis. They found that both methods produced similar *S*-wave velocities and layer depths. This could be particularly useful in the areas of lower earthquake seismicity, like the eastern and central United States, where few local earthquakes are insufficient to constrain high-resolution images of the near surface and/or upper crust. The novel method of isolating the effects of relative event–channel azimuth offers an independent way of investigating the average Rayleigh and Love phase velocities of the subsurface around the DAS fiber. The current results may be scattered by uncontrolled factors, such as uncharacterized small-scale local geology, detailed mapping of the FORESEE fiber depth, and importantly the unknown quality of the fiber-optic cable coupling within its concrete conduit. Because of this, other geophysical methods of subsurface exploration should be used in tandem with these analyses for greatest effect on large data sets such as the FORESEE lightning quakes.

Another implication of the novel azimuthal sensitivity analysis comes in the the depth dependence of the equations. This depth dependence could allow further development of this method to aid in the depth mapping of dark telecom fibers. For example, this work utilized thousands of DAS channels considered in two large groups. The investigation of smaller groups of channels may show stronger depth dependence, which could be used for comparatively high-resolution depth estimations. Understanding the average or local depth of a fiber-optic cable in the absence of original installation records can help new DAS installations view their data in a more complete context.

The numerical simulations of lightning quake events 26059 and 16333 add that observations do not show any evidence of electroseismically converted waves. This is probably due to the distance between the receiving DAS channels and the base of many of the lightning channels used in this study. Millisecond-duration-pulsed EM fields created by lightning may be very strong, but the frequency of the induced ES wave would theoretically be on the order of 1 kHz (Peng *et al.*, 2018). These waves, although they may exist, most likely attenuate very quickly with distance away from the source. The simulations in this study are not able to replicate sources of such a high central frequency, so we lose out on a perfect conceptual understanding of how exactly lightning's EM field would couple into the saturated ground. Future work focusing on the simulation of ES coupling of natural sources such as lightning should progress toward a computational framework capable of capturing the full high-frequency source physics. The simulations more robustly show that the lightning quakes are caused by acoustic-to-seismic coupling; however, it is important that the simulation code may not have captured the full physics of the acoustic sources. In a simplified view, lightning bolts can be seen as creating vertical acoustic line sources stretching from the ground to the clouds, with the strength of the acoustic source varying along that line with the temperature of the bolt. As the acoustic line propagates downward, it couples with the ground. Acoustic-to-seismic coupling occurs most efficiently at the angle of vertical incidence in which the slowness of the



Downloaded from http://pubs.geoscienceworld.org/ssa/bssa/article-pdf/doi/10.1785/0120230116/5983977/bssa-2023116.1.pdf
by Pennsylvania State University user

incident wave occurs near the Rayleigh-wave pole. At this angle, transmission energy can be orders of magnitude greater than at other incident angles. The distance at which this angle is achieved for a thunder source may not be a matter of simple trigonometry. Thunder refracts through the nonuniform atmosphere. The temperature-based refraction oftentimes bends upward propagating thunder back down toward the ground a great distance away from the bolt. Further complications can arise when the simplified line-source model of thunder is re-examined. Lightning bolts are, by the nature of their underlying physics, sources of tortuous geometry. This tortuous geometry can create branches or curve the bolt into the clouds where it stretches for many kilometers.

For future studies interested in the usage of lightning quakes as sources for seismic tomography, the complex geometry and acoustic propagation of lightning and thunder must be considered. However, for this study these complicated source and propagation mechanics likely only contributed to azimuthal uncertainty in normalized strain rates and simplistic results of the numerical modeling compared with the observed lightning quakes.

The FORESEE DAS array allows us to view lightning quake signals in high resolution. Numerical simulation of acoustic-to-seismic and ES wavefields show the apparent lack of significant ES signals in our lightning quake data. The high sample size of lightning quake events and the inherent azimuthal variation of expected DAS strain rates allows us to use novel angular analysis methods to identify compounded surface wave-induced normalized strain rates and estimate surface-wave phase velocities in the near-surface layer. All together, lightning remains an attractive candidate for near-surface characterization due to its frequent natural occurrence, high SNR, robust passive atmospheric measurement, and the relevance of the results to lightning safety systems and the human-inhabited critical zone (Cummins *et al.*, 1998; Lin and Langston, 2007; Arrowsmith *et al.*, 2010; Hinzen, 2012; Beroual and Fofana, 2016; Novoselov *et al.*, 2022). Around the world, almost 100 lightning strikes per second occur within around 2000 active thunderstorms (Beroual and Fofana, 2016). Many of these lightning-prone areas are bereft of natural seismicity, such as the central and eastern United States (Zhu and Stensrud, 2019). Lightning quakes may provide data to constrain high-resolution images of the near-surface in which earthquake data are insufficient.

## DATA AND RESOURCES

The 2019–2020 raw distributed acoustic sensing (DAS) waveform data from the Fiber Optic foR Environmental SEnsEing (FORESEE) array, including the waveforms of the 109 lightning quakes used in this study, is available at the following Penn State Data Commons link tinyurl.com/499mn4pa. Lightning data provided through a research agreement with Vaisala Inc. Requests for lightning data can be made through Vaisala Inc. at https://www.vaisala.com/en/lp/request-vaisala-lightning-data-research-use. All websites were last accessed in July 2021.

## DECLARATION OF COMPETING INTERESTS

The authors acknowledge that there are no conflicts of interests recorded.

## ACKNOWLEDGMENTS

The Fiber Optic foR Environmental SEnsEing (FORESEE) Array project gives its thanks to Chris Marone for his support in securing funding from the Penn State Institute of Natural Gas Research. The authors would also like to thank Todd Myers and Ken Miller at Penn State University and Thomas Coleman from Silixa, who helped the field setup. The detailed National Lightning Detection Network (NLDN) lightning data were generously provided by Vaisala. Color maps for many of the figures in this work were developed by Crameri *et al.* (2020).

## REFERENCES

Abegunawardana, S., J. A. P. Bodhika, U. Sonnadara, and M. Fernando (2016). Frequency analysis of thunder features, *33th International Conf. on Lightning Protection*, 25–30 September 2016, Estoril, Portugal, 1–5.

Albert, D. G., S. Taherzadeh, K. Attenborough, P. Boulanger, and S. N. Decato (2013). Ground vibrations produced by surface and near-surface explosions, *Appl. Acoust.* **74,** no. 11, 1279–1296, doi: 10.1016/j.apacoust.2013.03.006.

Arrowsmith, S. J., J. B. Johnson, D. P. Drob, and M. A. Hedlin (2010). The seismoacoustic wavefield: A new paradigm in studying geophysical phenomena, *Rev. Geophys.* **48,** no. 4, 1–23, doi: 10.1029/2010RG000335.

Beroual, A., and I. Fofana (2016). Lightning discharge, in *Discharge in Long Air Gaps Modelling and Applications*, IOP Publishing, Bristol, United Kingdom, 1–19, doi: 10.1088/978-0-7503-1236-3ch5.

Blumenthal, R. (2016). The explosive effects of lightning: What are the risks? *Acad. Forensic Pathol.* **6,** no. 1, 89–95, doi: 10.23907/2016.008.

Boggs, L. D., N. Liu, A. Nag, T. D. Walker, H. J. Christian, C. L. da Silva, M. Austin, F. Aguirre, and H. K. Rassoul (2021). Vertical temperature profile of natural lightning return strokes derived from optical spectra, *J. Geophys. Res.* **126,** no. 8, 1–15, doi: 10.1029/2020JD034438.

Crameri, F., G. E. Shephard, and P. J. Heron (2020). The misuse of colour in science communication, *Nat. Commun.* **11,** no. 1, 1–10, doi: 10.1038/s41467-020-19160-7.

Cummins, K. L., M. J. Murphy, E. A. Bardo, W. L. Hiscox, R. B. Pyle, and A. E. Pifer (1998). A combined TOA/MDF technology upgrade of the US National Lightning Detection Network, *J. Geophys. Res.* **103,** no. D8, 9035–9044, doi: 10.1029/98JD00153.

Czarny, R., and T. Zhu (2022). Estimating Rayleigh surface wave from ambient noise recorded by distributed acoustic sensing (DAS) dark fiber array in the city, in *SEG Technical Program Expanded Abstracts*, Houston, Texas, August 2022, 2133–2137, doi: 10.1190/image2022-3750564.1.

Dessler, A. J. (1973). Infrasonic thunder, *J. Geophys. Res.* **78,** no. 12, 1889–1896, doi: 10.1029/jc078i012p01889.

Dou, S., N. Lindsey, A. M. Wagner, T. M. Daley, B. Freifeld, M. Robertson, J. Peterson, C. Ulrich, E. R. Martin, and J. B. Ajo-Franklin (2017). Distributed acoustic sensing for seismic monitoring of the near surface: A traffic-noise interferometry case study, *Sci. Rep.* **7,** no. 1, 1–12, doi: 10.1038/s41598-017-11986-4.



Downloaded from http://pubs.geoscienceworld.org/ssa/bssa/article-pdf/doi/10.1785/0120230116/5983977/bssa-2023116.1.pdf
by Pennsylvania State University user

Dupuis, J. C., K. E. Butler, and A. W. Kepic (2007). Seismoelectric imaging of the vadose zone of a sand aquifer, *Geophysics* **72,** no. 6, 81–85, doi: 10.1190/1.2773780.

Dwyer, J. R., and M. A. Uman (2014). The physics of lightning, *Phys. Rep.* **534,** no. 4, 147–241, doi: 10.1016/j.physrep.2013.09.004.

Espinosa, A. F., P. J. Sierra, and W. V. Mickey (1968). Seismic waves generated by sonic booms: A geoacoustical problem, *J. Acoust. Soc. Am.* **44,** no. 4, 1074–1082, doi: 10.1121/1.1911198.

Farges, T., and E. Blanc (2010). Characteristics of infrasound from lightning and sprites near thunderstorm areas, *J. Geophys. Res.* **115,** no. 6, 1–17, doi: 10.1029/2009JA014700.

Few, A. (1969). Power spectrum of thunder, *J. Geophys. Res.* **74,** no. 28, 6926–6934, doi: 10.1029/jc074i028p06926.

Fischer, R. A. (2021). *Seismoelectric Exploration: Theory, Experiments, and Applications*, N. Grobbe, A. Revil, Z. Zhu, and E. Slob (Editors), First Ed., American Geophysical Union and John Wiley and Sons Inc, Washington D.C. and Hoboken, New Jersey.

Gao, Y., M. Wang, H. Hu, and X. Chen (2017). Seismoelectric responses to an explosive source in a fluid above a fluid-saturated porous medium, *J. Geophys. Res.* **122,** no. 9, 7190–7218. doi:10.1002/2016JB013703.

Garambois, S., and M. Dietrich (2001). Seismoelectric wave conversions in porous media: Field measurements and transfer function analysis, *Geophysics* **66,** no. 5, 1417–1430, doi: 10.1190/1.1487087.

Garcés, M. A., R. A. Hansen, and K. G. Lindquist (1998). Travel times for infra-sonic waves propagating in a stratified atmosphere, *Geophys. J. Int.* **135,** no. 1, 255–263, doi: 10.1046/j.1365-246X.1998.00618.x.

Graneau, P. (1989). The cause of thunder, *J. Phys. D* **22,** no. 8, 1083–1094, doi: 10.1088/0022-3727/22/8/012.

Haartsen, M. W., and S. R. Pride (1997). Electroseismic waves from point sources in layered media, *J. Geophys. Res.* **102,** no. 11, 24,745–24,769, doi: 10.1029/97jb02936.

Hill, J. D. (2012). The mechanisms of lightning leader propagation and ground attachment, Unpublished *Doctoral Dissertation*, University of Florida.

Hinzen, K. G. (2012). Seismological analysis of a lightning strike, *Seismol. Res. Lett.* **83,** no. 3, 492–497, doi: 10.1785/gssrl.83.3.492.

Hone, S., and T. Zhu (2021). Seismic observations of four thunderstorms using an underground fiber-optic array, *Seismol. Res. Lett.* **92,** no. 4, 2389–2398, doi: 10.1785/0220200264.

Kappus, M. E., and F. L. Vernon (1991). Acoustic signature of thunder from seismic records, *J. Geophys. Res.* **96,** no. D6, 10,989, doi: 10.1029/91JD00789.

Kennett, B. (2023). Interacting seismic waveguides: Multimode surface waves and leaking modes, *Seismica* **2,** no. 1, 1–12, doi: 10.26443/seismica.v2i1.282.

Kitov, I., J. Murphy, O. Kusnetsov, B. Barker, and N. Nedoshivin (1997). An analysis of seismic and acoustic signals measured from a series of atmospheric and near-surface explosions, *Bull. Seismol. Soc. Am.* **87,** no. 6, 1553–1562.

Krider, E. P., and R. H. Wetmore (1987). Upward streamers produced by a lightning strike to radio transmission towers, *J. Geophys. Res.* **92,** no. D8, 9859, doi: 10.1029/jd092id08p09859.

Kulessa, B., T. Murray, and D. Rippin (2006). Active seismoelectric exploration of glaciers, *Geophys. Res. Lett.* **33,** no. 7, 2–5, doi: 10.1029/2006GL025758.

Lamb, O. D., J. M. Lees, and D. C. Bowman (2018). Detecting lightning infra-sound using a high-altitude balloon, *Geophys. Res. Lett.* **45,** no. 14, 7176–7183, doi: 10.1029/2018GL078401.

Langston, C. A. (2004). Seismic ground motions from a bolide shock wave, *J. Geophys. Res.* **109,** no. 12, 1–23, doi: 10.1029/2004JB003167.

Lellouch, A., N. J. Lindsey, W. L. Ellsworth, and B. L. Biondi (2020). Comparison between distributed acoustic sensing and geophones: Downhole microseismic monitoring of the FORGE geothermal experiment, *Seismol. Res. Lett.* **91,** no. 6, 3256–3268, doi: 10.1785/0220200149.

Lin, T. L., and C. A. Langston (2007). Infrasound from thunder: A natural seismic source, *Geophys. Res. Lett.* **34,** no. 14, 1–6, doi: 10.1029/2007GL030404.

Lin, T. L., and C. A. Langston (2009a). Thunder-induced ground motions: 1. Observations, *J. Geophys. Res.* **114,** no. 4, 1–19, doi: 10.1029/2008JB005769.

Lin, T. L., and C. A. Langston (2009b). Thunder-induced ground motions: 2. Site characterization, *J. Geophys. Res.* **114,** no. 4, 1–11, doi: 10.1029/2008JB005770.

Lindsey, N. J., and E. R. Martin (2021). Fiber-optic seismology, *Annu. Rev. Earth Planet. Sci.* **49,** 309–336, doi: 10.1146/10.1146/annurev-earth-072420-065213.

Liu, Y., D. Smeulders, Y. Su, and X. Tang (2018). Seismoelectric interface electromagnetic wave characteristics for the finite offset vertical seismoelectric profiling configuration: Theoretical modeling and experiment verification, *J. Acoust. Soc. Am.* **143,** no. 1, EL13–EL18, doi: 10.1121/1.5020261.

Lu, W., L. Chen, Y. Zhang, Y. Ma, Y. Gao, Q. Yin, S. Chen, Z. Huang, and Y. Zhang (2012). Characteristics of unconnected upward leaders initiated from tall structures observed in Guangzhou, *J. Geophys. Res.* **117,** no. 19, 1–12, doi: 10.1029/2012JD018035.

Martin, E. R., N. J. Lindsey, J. B. Ajo-Franklin, and B. L. Biondi (2021). Introduction to interferometry of fiber-optic strain measurements, in *Distributed Acoustic Sensing in Geophysics: Methods and Applications*, Y. Li, M. Karrenbach, and J. B. Ajo-Franklin (Editors), First Ed., Geophysical Monograph Series, American Geophysical Union, Washington D.C., 113–129, doi: 10.1002/9781119521808.ch09.

Nag, A., M. J. Murphy, W. Schulz, and K. L. Cummins (2015). Lightning locating systems: Insights on characteristics and validation techniques, *Earth Space Sci.* **2,** 65–93, doi: 10.1002/2014EA000051.

Nieckarz, Z., A. Kulak, S. Zieba, and A. Odzimek (2011). Cloud-to-ground lightning dipole moment from simultaneous observations by ELF receiver and combined direction finding and time-of-arrival lightning detection system, *J. Geophys. Res.* **116,** no. D8, 1–9, doi: 10.1029/2010JD014736.

Novoselov, A., M. Dorninger, G. Diendorfer, G. Bokelmann, and , and The AlpArray Working Group (2022). Seismoacoustic study of thunder and lightning using the AlpArray, *Seismol. Res. Lett.* doi: 10.1785/0220220064.

Novoselov, A., F. Fuchs, and G. Bokelmann (2020). Acoustic-to-seismic ground coupling: Coupling efficiency and inferring near-surface properties, *Geophys. J. Int.* **223,** no. 1, 144–160, doi: 10.1093/gji/ggaa304.

Nucci, C. A., G. Diendorfer, M. A. Uman, F. Rachidi, M. Ianoz, and C. Mazzetti (1990). Lightning return stroke current models with



Downloaded from http://pubs.geoscienceworld.org/ssa/bssa/article-pdf/doi/10.1785/0120230116/5983977/bssa-2023116.1.pdf
by Pennsylvania State University user

specified channel-base current: a review and comparison, *J. Geophys. Res.* **95,** no. 90, 20,395–20,408.

Onaga, H., and J. H. Rindel (2007). Acoustic characteristics of urban streets in relation to scattering caused by building facades, *Appl. Acoust.* **68,** no. 3, 310–325, doi: 10.1016/j.apacoust.2006.01.010.

Peng, R., B. Di, J. Wei, P. Ding, Z. Liu, B. Guan, and S. Huang (2018). Signal characteristics of electroseismic conversion, *J. Geophys. Eng.* **15,** no. 2, 377–385, doi: 10.1088/1742-2140/aaa0a2.

Potylitsyn, V. S., G. Y. Shaydurov, D. S. Kudinov, E. A. Kokhonkova, and P. V. Balandin (2019). Comparative analysis of conventional seismic survey with passive seismoelectric exploration at gas condensate field, *Int. J. Geomate* **17,** no. 63, 347–352, doi: 10.21660/2019.63.78699.

Pride, S. R. (1994). Governing equations for the coupled electromagnetics and acoustics of porous media, *Phys. Rev. B* **50,** no. 21, 15,678–15,696, doi: 10.1103/PhysRevB.50.15678.

Pride, S. R., and M. W. Haartsen (1996). Electroseismic wave properties, *J. Acoust. Soc. Am.* **100,** no. 3, 1301–1315, doi: 10.1121/1.416018.

Rodríguez Tribaldos, V., and J. B. Ajo-Franklin (2021). Aquifer monitoring using ambient seismic noise recorded with distributed acoustic sensing (DAS) deployed on dark fiber, *J. Geophys. Res.* **126,** no. 4, 1–20, doi: 10.1029/2020JB021004.

Sabatier, J. M., and R. Raspet (1988). Investigation of possibility of damage from the acoustically coupled seismic waveform from blast and artillery, *J. Acoust. Soc. Am.* **84,** no. 4, 1478–1482, doi: 10.1121/1.396593.

Shoory, A., F. Rachidi, F. Delfino, R. Procopio, and M. Rossi (2011). Lightning electromagnetic radiation over a stratified conducting ground: 2. Validity of simplified approaches, *J. Geophys. Res.* **116,** no. 11, doi: 10.1029/2010JD015078.

Slob, E., and M. Mulder (2016). Seismoelectromagnetic homogeneous space Green's functions, *Geophysics* **81,** no. 4, F27–F40, doi: 10.1190/geo2015-0337.1.

Solomos, G., V. Karlos, and M. Larcher (2016). *Analysis of Blast Parameters in the Near-Field for Spherical Free-Air Explosions, Technical Rept.*, Joint Research Center, Ispra, Varese, Italy, 21027.

Tran, M. D., V. A. Rakov, and S. Mallick (2014). A negative cloud-to-ground flash showing a number of new and rarely observed features, *Geophys. Res. Lett.* **41,** no. 18, 6523–6529, doi: 10.1002/2014GL061169.

Walter, F., D. Gräff, F. Lindner, P. Paitz, M. Köpfli, M. Chmiel, and A. Fichtner (2020). Distributed acoustic sensing of microseismic sources and wave propagation in glaciated terrain, *Nat. Commun.* **11,** no. 1, 1–10, doi: 10.1038/s41467-020-15824-6.

Wang, D., Y. Gao, C. Yao, B. Wang, and M. Wang (2020). Seismoelectric and electroseismic responses to a point source in a marine stratified model, *Geophys. Prospect.* **68,** no. 6, 1958–1979, doi: 10.1111/1365-2478.12948.

White, B. S., and M. Zhou (2006). Electroseismic prospecting in layered media, *SIAM J. Appl. Math.* **67,** no. 1, 69–98, doi: 10.1137/050633603.

Zheng, X. Z., H. Ren, K. E. Butler, H. Zhang, Y. C. Sun, W. Zhang, Q. Huang, and X. Chen (2021). Seismoelectric and electroseismic modeling in stratified porous media with a shallow or ground surface source, *J. Geophys. Res.* **126,** no. 9, 1–70, doi: 10.1029/2021JB021950.

Zhu, T., and D. J. Stensrud (2019). Characterizing thunder-induced ground motions using fiber-optic distributed acoustic sensing array, *J. Geophys. Res.* **124,** no. 23, 12,810–12,823, doi: 10.1029/2019JD031453.

Zhu, T., J. Shen, and E. R. Martin (2021). Sensing earth and environment dynamics by telecommunication fiber-optic sensors: An urban experiment in Pennsylvania, USA, *Solid Earth* **12,** no. 1, 219–235, doi: 10.5194/se-12-219-2021.

Zhu, Z., M. N. Toksöz, and D. R. Burns (2008). Electroseismic and seismoelectric measurements of rock samples in a water tank, *Geophysics* **73,** no. 5, 1–25, doi: 10.1190/1.2952570.

**Manuscript received 31 May 2023**
**Published online 10 October 2023**



Downloaded from http://pubs.geoscienceworld.org/ssa/bssa/article-pdf/doi/10.1785/0120230116/5983977/bssa-2023116.1.pdf
by Pennsylvania State University user